Industrial Chemistry & Materials

工业化学与材料 (英文)
(Online) ISSN 2755-2500
(Print) ISSN 2755-2608
CN 10-2056/TQ
rsc.li/icm

Volume 4 Number 2 March 2026

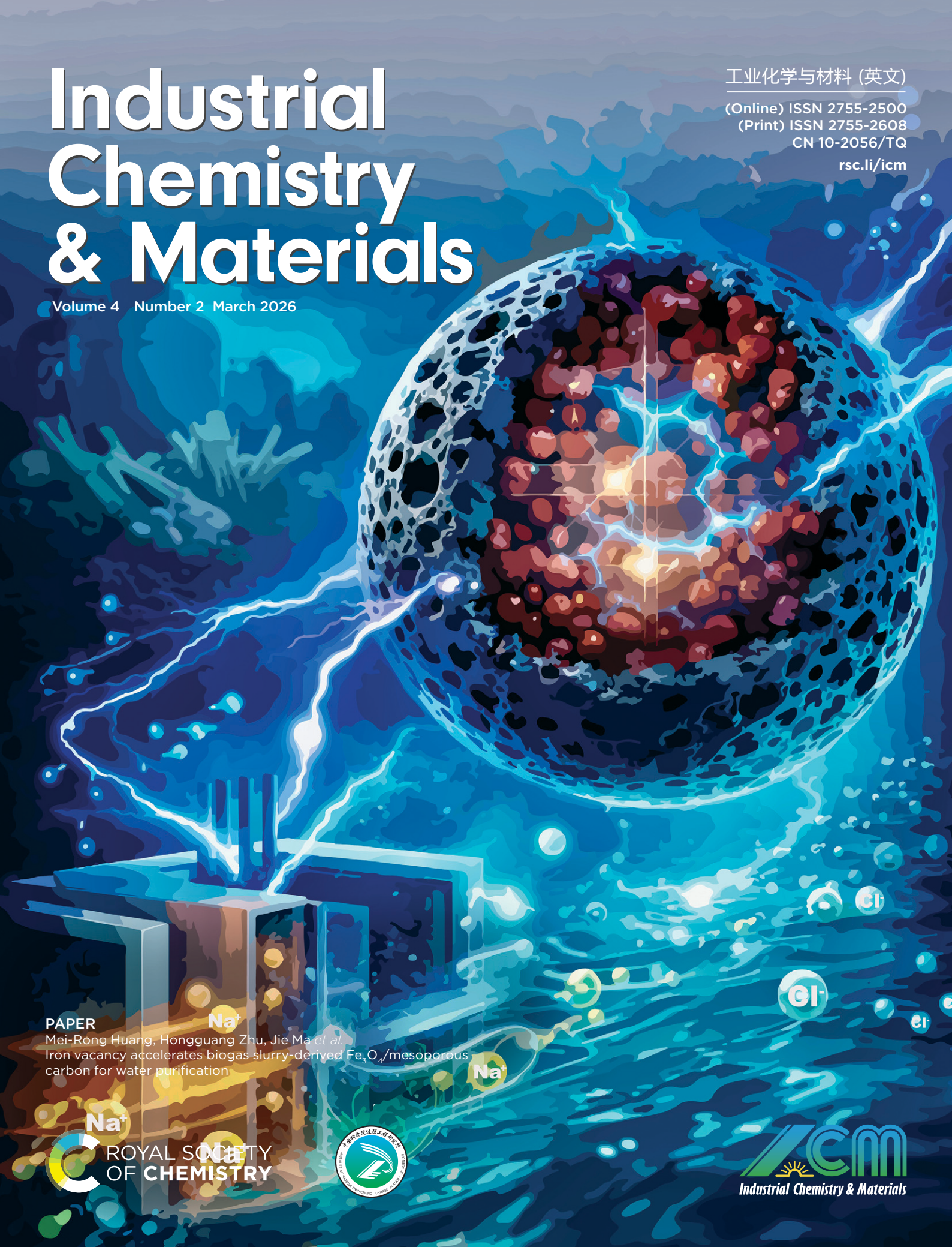

PAPER

Mei-Rong Huang, Hongguang Zhu, Jie Ma *et al.*
Iron vacancy accelerates biogas slurry-derived Fe_3O_4/mesoporous carbon for water purification

ROYAL SOCIETY OF CHEMISTRY

Industrial Chemistry & Materials

Industrial Chemistry & Materials

ROYAL SOCIETY OF CHEMISTRY

PAPER

View Article Online
View Journal | View Issue

Cite this: *Ind. Chem. Mater.*, 2026, **4**, 172

Iron vacancy accelerates biogas slurry-derived Fe_3O_4/mesoporous carbon for water purification

Liangmei Rao,[a] Jinfeng Chen,[a] Mei-Rong Huang,*[a] Hongguang Zhu,*[cd] Fei Yu [e] and Jie Ma *[abe]

Received 24th June 2025,
Accepted 11th October 2025

DOI: 10.1039/d5im00117j

rsc.li/icm

Fe_3O_4 is a promising transition metal oxide for ion removal owing to its high theoretical capacity, hydrophilicity, and non-toxicity, but its structural instability during ion insertion–extraction limits practical application. Here, Fe_3O_4 was integrated with mesoporous carbon derived from biogas slurry to enhance conductivity and sustainability, followed by alkaline etching to introduce abundant iron vacancies (VFO). The resulting VFO-C composite exhibits accelerated charge transfer, numerous intercalation-active sites, and superior electrochemical stability. At 1.6 V, the material achieved a desalination capacity of 126 mg g^{-1} and retained 96.6% of its initial capacity after prolonged cycling. This performance surpasses conventional Fe_3O_4 electrodes, highlighting the synergistic benefits of defect engineering and waste-derived carbon. The strategy not only advances high-efficiency and durable capacitive deionization but also broadens potential applications in energy storage systems such as supercapacitors and batteries.

Keywords: Iron vacancy; Biogas slurry; Fe_3O_4; Capacitive deionization.

1 Introduction

Recently, Fe_3O_4 (magnetite) has garnered significant attention in the field of ion removal due to its favorable electrochemical properties, non-toxicity, and high theoretical capacity,[1,2] as well as high corrosion resistance, low cost, natural abundance,[3,4] and environmental friendliness in terms of long-term economics.[5–8] However, despite having been so attractive, the drastic volume change inevitably caused during the ion embedding and detachment process leads to a significant challenge to the material's structural stability, low conductivity of pristine Fe_3O_4 also limits the breakthrough in the material capacity.[9–12] Therefore, improving the structural stability of Fe_3O_4 through precise microstructural control has become an important research focus in this area.

To overcome these challenges, innovative approaches have been developed. Researchers have shortened ion diffusion pathways, alleviated volume stress, and increased surface area for enhanced electrochemical reactions by fabricating Fe_3O_4 into nanoparticles or porous structures. Also, strategy of coating Fe_3O_4 with conductive materials such as graphene, carbon nanotubes, or conductive polymers has improved conductivity and enhanced the stability of the material. Studies have shown that introducing specific lattice defects, such as iron vacancies, has significantly enhanced the intrinsic reactivity and cycling stability of Fe_3O_4. Among these strategies, creating vacancies has been shown to enhance ORR activity by optimizing the adsorption of oxygen intermediates and facilitating electron transfer.[13] It also mitigates the volume expansion associated with ion insertion, thereby enhancing the structural stability of the material.[14,15] Furthermore, iron vacancies can improve charge distribution and electrochemical reactivity, leading to superior ion removal efficiency.[16,17] For example, researchers have successfully synthesized iron vacancy-rich Fe_3O_4 using an alkaline etching strategy, demonstrating its excellent performance in electrochemical desalination.[18] Despite the enhanced performance brought by iron vacancies, the long-term electrochemical stability of these materials, especially under repetitive cycling, highlights the need for complementary strategies, such as the incorporation of green conductive materials.

Biochar, a low-cost, eco-friendly carbon material with widespread availability, has shown promising potential in various electrochemical applications.[19] Furthermore, growing environmental awareness and the need for sustainable

[a] *Research Center for Environmental Functional Materials, State Key Laboratory of Water Pollution Control and Green Resource Recycling, College of Environmental Science and Engineering, Tongji University, Shanghai, 200092, P. R. China. E-mail: jma@tongji.edu.cn, huangmeirong@tongji.edu.cn*
[b] *Water Resources and Water Environment Engineering Technology Center, Xinjiang Key Laboratory of Engineering Materials and Structural Safety, School of Civil Engineering, Kashi University, Kashi 844000, P. R. China*
[c] *Shanghai Institute of Pollution Control and Ecological Security, Shanghai 200092, P. R. China. E-mail: zhuhg@tongji.edu.cn*
[d] *Modern Agricultural Science & Engineering, Institute of Biomass Energy Research Centre, Tongji University, Shanghai 201804, P. R. China*
[e] *College of Oceanography and Ecological Science, Shanghai Ocean University, No 999, Huchenghuan Road, Shanghai, 201306, P. R. China*

resource utilization have driven the development of green materials in modern materials science. Particularly, biochar derived from anaerobic fermentation residues, such as biogas slurry, provides an effective means of recycling waste into useful resources, thereby promoting a circular economy.[20,21] Incorporating biogas slurry carbon into Fe_3O_4-based systems compensates for conductivity limitations of Fe_3O_4, offers additional active sites, and enhances the overall electrochemical performance and cycle life.[22,23] As a green carbon source, biogas slurry-derived carbon also contributes to reducing the carbon footprint of material production, facilitating a more sustainable, low-cost production process. As summarized in Table S1, capacitive deionization (CDI) technique exhibits a markedly lower specific energy consumption (~0.2–1.0 kWh m^{-3}) for low-salinity water compared to reverse osmosis (0.5–4 kWh m^{-3}) and membrane distillation (0.6–1.8 kWh m^{-3} electrical plus significant thermal demand), underscoring its energy-saving advantage for sustainable desalination.

This study presents an innovative strategy that integrates Fe_3O_4 with abundant iron vacancies (VFO) and mesoporous carbon derived from biogas slurry (C). The materials were designed to address the intrinsic performance limitations of Fe_3O_4, such as poor conductivity and structural instability, while simultaneously promoting sustainable material development. By incorporating biogas slurry-derived carbon, the conductivity of the composite was significantly improved, and additional active sites were provided, enhancing the

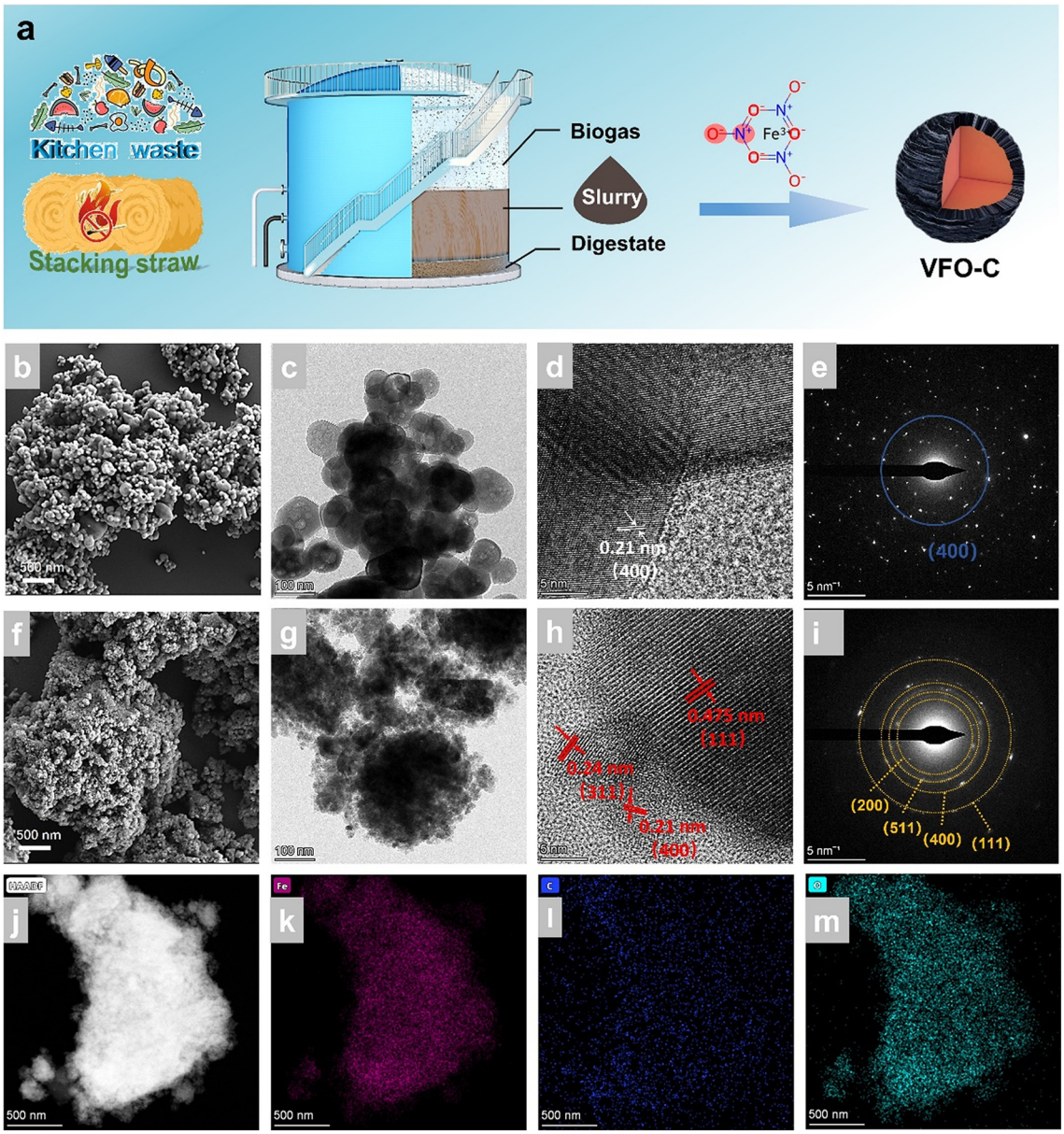

Fig. 1 (a) Schematic illustration of the source of VFO-C material preparation and the preparation process; SEM, TEM, HRTEM and SAED images of Fe_3O_4-C (b–e) and VFO-C (f–i), respectively. EDS mapping image of VFO-C (j–m).

overall electrochemical performance. The introduction of iron vacancies further optimized ion transport and mitigated volume expansion during ion insertion and extraction. The resulting composite material, VFO-C, demonstrated exceptional performance in various tests, including a high ion removal efficiency of 126 mg g^{-1} at 1.6 V during electrochemical desalination and remarkable cycling stability, retaining 96.6% of its capacity after recirculating desalination. Additionally, the material exhibited a low capacity decay rate during repeated charge–discharge cycles, confirming its strong electrochemical stability. These results highlight the effectiveness of combining defect engineering with sustainable carbon materials, addressing both technical challenges and environmental concerns. The synergistic integration of iron vacancies and biogas slurry-derived carbon not only enhances the electrochemical properties of Fe_3O_4 but also aligns with green chemistry principles, offering a pathway for the development of next-generation materials. This strategy holds significant potential for practical applications in ion removal technologies and energy storage systems.

2 Results and discussion

2.1 Characterization of Fe_3O_4-C and VFO-C

The morphology and microstructure of Fe_3O_4-C and VFO-C heterostructure were characterized by SEM and TEM. As can be seen from the SEM images of Fig. 1b and f, the NaOH-etched material exhibits a more homogeneous morphology. This improved homogeneity may be attributed to the behavior of Al_2O_3 under alkaline conditions. Al_2O_3 forms hydrated particles in solution, whose surface charge can become either positive or negative depending on protonation. The loss of H^+ from surface hydroxyl groups, forming negatively charged AlO_2^-, introduces electrostatic repulsion between particles, thereby suppressing agglomeration.[24,25] Consequently, the alkali-treated material exhibits greater uniformity and a smaller average particle size. Fig. 1c and g show more clearly that the material forms spherical-like particles and some pores on the surface, and this morphology is conducive to mitigating the volume expansion induced by the redox reaction of ions on the surface of the material as a result of repeated charging and discharging during the desalination process.[26,27] Meanwhile, the constructed VFO-C also exhibits a high degree of homogeneity in the TEM images. The characteristic lattice streaks of Fe_3O_4 can be seen by HRTEM with a lattice spacing of 2.4 Å, which belongs to the crystallographic plane (311),[28] as well as a characteristic lattice belonging to the crystallographic plane (400) at a lattice spacing of 2.1 Å. After etching, the (111) crystal face is more clearly characterized, showing a uniform lattice spacing of about 4.75 Å.[29] Meanwhile, these features are also reflected in the SAED as shown in Fig. 1e and i. HADDF images (Fig. 1j and k) show high-resolution compositional distributions of VFO-C, which corroborating its composite structure.

$$Al_2O_3 + 2NaOH + 3H_2O \rightarrow 2Na[Al(OH)_4]$$

Contact angle of electrode materials plays a pivotal role in determining the ion transport efficiency and adsorption capacity in capacitive deionization. Hydrophilic materials, with their lower contact angles, improve deionization performance by enhancing water–electrode interaction and reducing pore blockage.[30,31] In contrast, hydrophobic materials limit ion transfer and reduce the overall efficiency. We tested the contact angle and both of the composites exhibited less than 40° in Fig. 2a and b, which is favorable for subsequent CDI process, and an average contact angle of around 30° after etching. This also indicates a change in hydrophilicity with the increase of oxygen-containing functional groups on the surface of the material. Upon comparing the BET results before and after impregnation with nanoparticles in Fig. 2d, there was an apparent increases in surface area and a widening in pore size distribution, possibly due to the alkaline environment accelerating the dissolution of small inorganic components on the surface or inside the material,[32,33] and also due to the fact that alkali can dissolve a portion of the AlO_2^- bonds. This dissolving effect likewise produces more pores, thus increasing the specific surface area. Diffraction peaks in Fig. 2e observed at 2θ values of approximately 30°, 35°, 43°, 53°, 57°, and 62° correspond to the (220), (311), (400), (422), (511), and (440) crystallographic planes of magnetite (Fe_3O_4), respectively, consistent with the standard JCPDS card No. 19-0629.[34] The absence of distinct carbon peaks around 25° may be attributed to the amorphous nature of carbon, and potential peak overlap with Fe_3O_4.[35,36] XPS was used to compare the change in valence binding energy at the surface of the material. As can be seen from total XPS spectra in Fig. 2f, there is not much difference between the two, indicating that the overall elements have not changed much. In the Fe 2p spectra in Fig. 2g, the Fe^{II} $2p_{3/2}$ peaks of the Fe_3O_4 samples usually appeared near 710.6 eV, and the Fe^{II} $2p_{1/2}$ peaks appeared around 723.1 eV. After the introduction of iron vacancies, these peaks changed significantly.[37,38] Specifically, the Fe^{II} $2p_{3/2}$ peak position is shifted to the high-energy side by about 0.3 eV and appears at 710.3 eV, while the Fe^{II} $2p_{1/2}$ peak is shifted to the high-energy side by almost 1.0 eV and appears at 724.1 eV.[39,40] This change in peak position suggests that the introduction of iron vacancies leads to a change in the local electronic environment, which affects the binding energy of Fe atoms. In terms of intensity, the overall intensity of the Fe^{III} 2p spectra decreased after the introduction of iron vacancies. This suggests that iron vacancies reduce the number of Fe^{III} atoms, leading to a weakened XPS signal. At the same time, we observed a change in the intensity of the satellite peaks in the Fe 2p spectra. The Fe^{III} $2p_{3/2}$ satellite peak of Fe_3O_4, which usually appears around 718.8 eV, was significantly enhanced in the samples with the introduction of iron vacancies.[41,42] This change further supports the idea that iron vacancies affect the electronic structure and local environment of Fe atoms.[43]

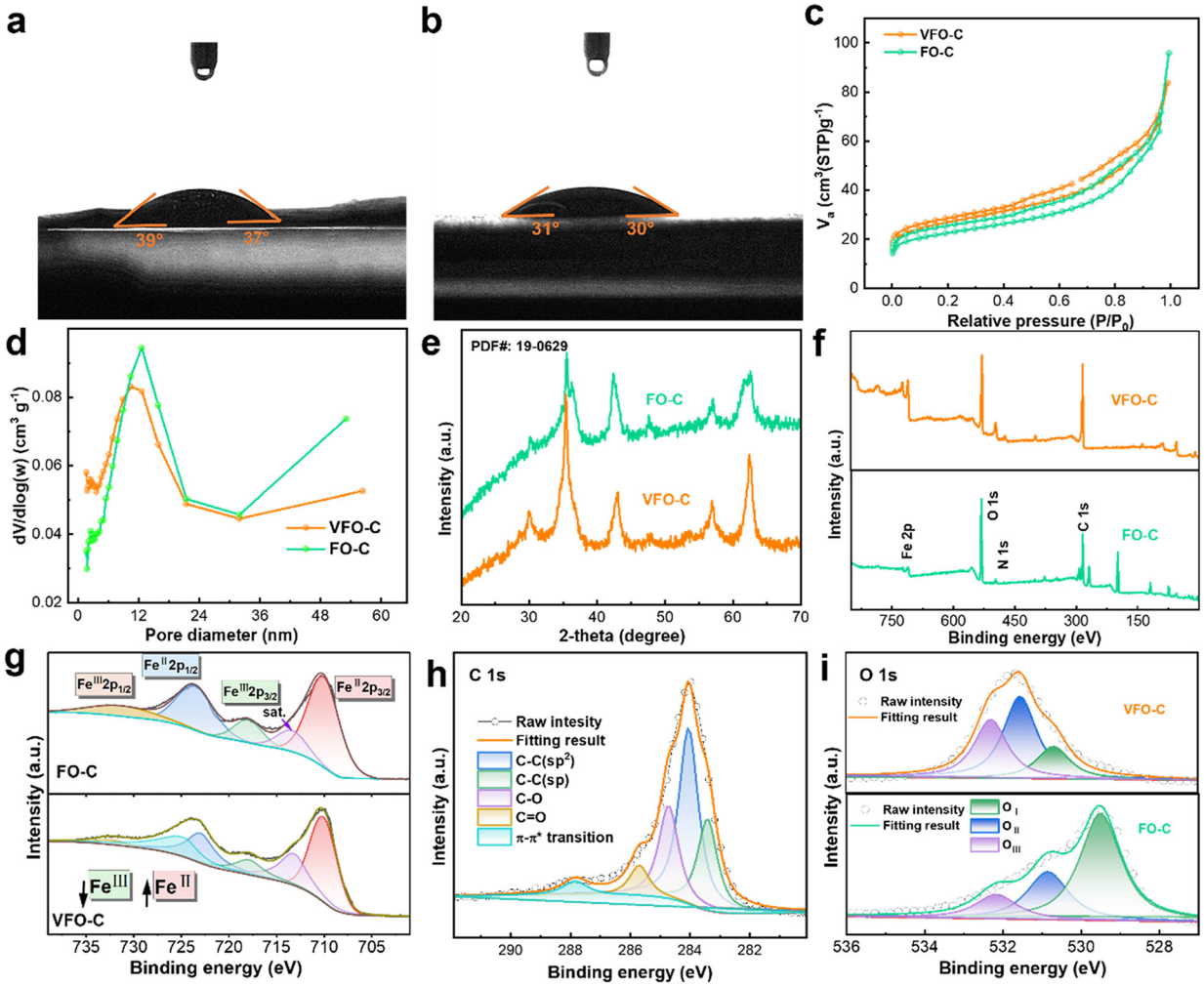

Fig. 2 Contact angles of Fe_3O_4-C (a) and VFO-C (b); N_2 adsorption isotherms (c) and pore size distributions (d) for Fe_3O_4-C and VFO-C; XRD patterns (e) and XPS survey spectra (f) of Fe_3O_4-C, VFO-C; high-resolution comparation Fe 2p (g), C 1s (h) and O 1s (i) of Fe_3O_4-C and VFO-C, respectively.

O 1s spectra also show significant changes after the introduction of iron vacancies. In the Fe_3O_4 samples, the O 1s peak usually appeared at 530.0 eV, representing the oxygen in the oxide. When iron vacancies were introduced, the position of the O 1s peak showed a slight change and shifted to the low-energy side by about 0.2 eV, appearing at 529.8 eV.[44] This change may be due to the change in the electronic environment around the oxygen atom caused by the iron vacancy, resulting in a change in the binding energy. In addition, a new shoulder peak appeared in the O 1s spectrum, located near 531.5 eV. This shoulder peak may correspond to the presence of surface hydroxyl groups or adsorbed oxygen. The introduction of iron vacancies may have increased the number of these surface species, leading to the appearance of a new shoulder peak in the O 1s spectrum.[45,46] By XPS spectroscopy, we found that the introduction of iron vacancies significantly affected the electronic structure and surface chemical properties of Fe_3O_4. Changes in peak positions, peak shapes, and intensities in the $Fe^{II/III}$ 2p and O 1s spectra indicate that iron vacancies caused significant changes in the local environment.[39,40] These changes further suggest that the introduction of iron vacancies can effectively modulate the physicochemical properties of Fe_3O_4, providing new possibilities for optimizing its performance in various applications.

2.2 Electrochemical properties of VFO-C

We performed cyclic voltammetry (CV) tests on Fe_3O_4-C and VFO-C in 1 M NaCl electrolyte. For the Fe_3O_4-C samples, the CV curves showed weak redox peaks in the potential range of −0.6 to 0.6 V, indicating low electrochemical activity. However, the CV curves showed more pronounced redox peaks, especially at −0.15 V and 0.15 V, which implied VFO-C were introduced. This suggests that the presence of iron vacancies significantly enhances the electrochemical activity of the materials, possibly due to more active sites and higher electronic conductivity.[47,48] The peak changes of CV curves for VFO-C were analyzed in detail at different sweep speeds (1 mV s^{-1} to 50 mV s^{-1}) in Fig. 3b, where analysis using the

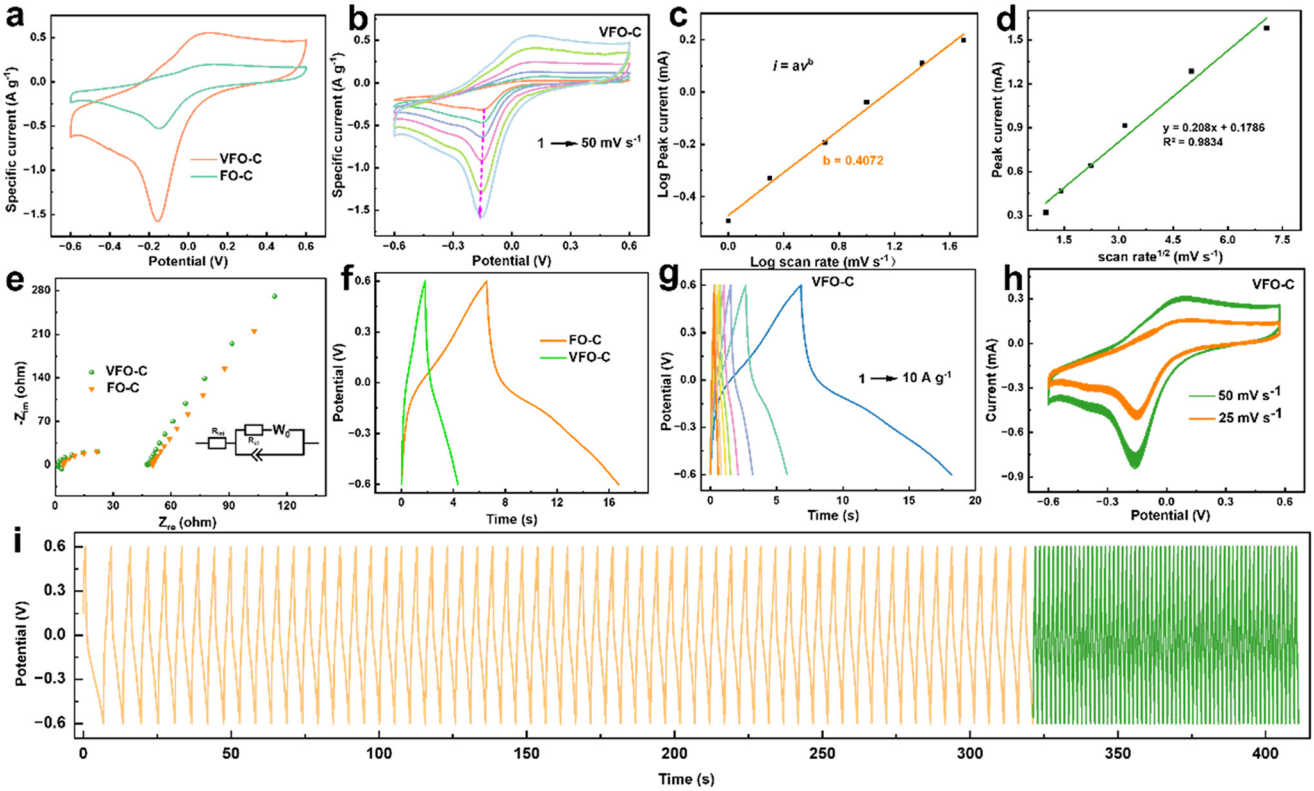

Fig. 3 Electrochemical performances of VFO-C. (a) CV curves at 50 mV s^{-1} of Fe_3O_4-C and VFO-C; (b) CV curves at 1–50 mV s^{-1}; (c) *b*-value calculations; (d) the relationship between peak current and $v^{1/2}$; (e) Nyquist plots; (f) GCD curves at 1 A g^{-1} of Fe_3O_4-C and VFO-C; (g) GCD curves at 1–10 A g^{-1}; (h) 100 CV cycles curves at 25 and 50 mV s^{-1}; (i) 60 GCD cycles curves at 1 and 2 A g^{-1}.

Tafel equation revealed b values was 0.4072, less than 0.5. This finding underscores its promising battery performance characteristics.[49] These attributes VFO-C enhanced conductivity and structural stability facilitate efficient charge transfer and minimize electrode polarization effects during cycling. The electrochemical impedance spectroscopy (EIS) test results show that the material with the introduced iron vacancies has a lower charge transfer resistance (R_{ct}) of about 20 Ω, while the R_{ct} of the Fe_3O_4-C is about 40 Ω. In addition, the Warburg impedance (Z_w) of the VFO-C is also lower, which suggests that it has a better ion diffusion performance.

In the constant-current charge–discharge test, VFO-C exhibits higher specific capacitance and better cycling stability. At a current density of 1 A g^{-1}, the specific capacitance of VFO-C is 220 F g^{-1}, while that of the Fe_3O_4-C is only 160 F g^{-1}. The specific capacitance of VFO-C stays high at different current densities (from 1 A g^{-1} to 10 A g^{-1}) and decays less at high current densities, indicating its excellent multiplicity performance. After 50 CV scans in both 25 mV s^{-1} and 50 mV s^{-1} in Fig. 3h, the shape and peak intensity of the CV curves remain stable, with a specific capacitance retention rate of more than 90%. This also indicates that the introduction of iron vacancies significantly improves the cyclic stability of the material. VFO-C were subjected to continuous cycling of charge and discharge for 60 cycles under current densities of 1 A g^{-1} and 2 A g^{-1}. Remarkably, VFO-C maintained their stability throughout the testing period. This endurance underscores their robust electrochemical performance and suggests their potential for applications requiring long-term cycling durability.

2.3 Desalination performance

Desalination performance of VFO-C and Fe_3O_4-C under various voltage conditions were investigated. Under constant voltage mode, the electrosorption performance of VFO-C was evaluated at applied voltages of 1.2, 1.4, and 1.6 V, with both adsorption and desorption durations set to 30 min. As shown in Fig. 4a and S5, the desalination performance of VFO-C exhibited distinct trends at different voltage levels. With increasing voltage, the desalination efficiency of VFO-C was significantly enhanced. However, within a certain voltage range, the performance improvement induced by voltage elevation gradually diminished. At the relatively low voltage of 1.6 V, VFO-C already demonstrated high desalination efficiency and a distinct performance advantage over Fe_3O_4-C. Although further enhancement was observed at the higher voltage of 1.8 V (Fig. S4), the incremental gain was relatively limited, indicating that the performance benefits of increasing voltage have an upper threshold. The high desalination efficiency at lower voltages can be attributed to a well-regulated electrochemical process that facilitates efficient

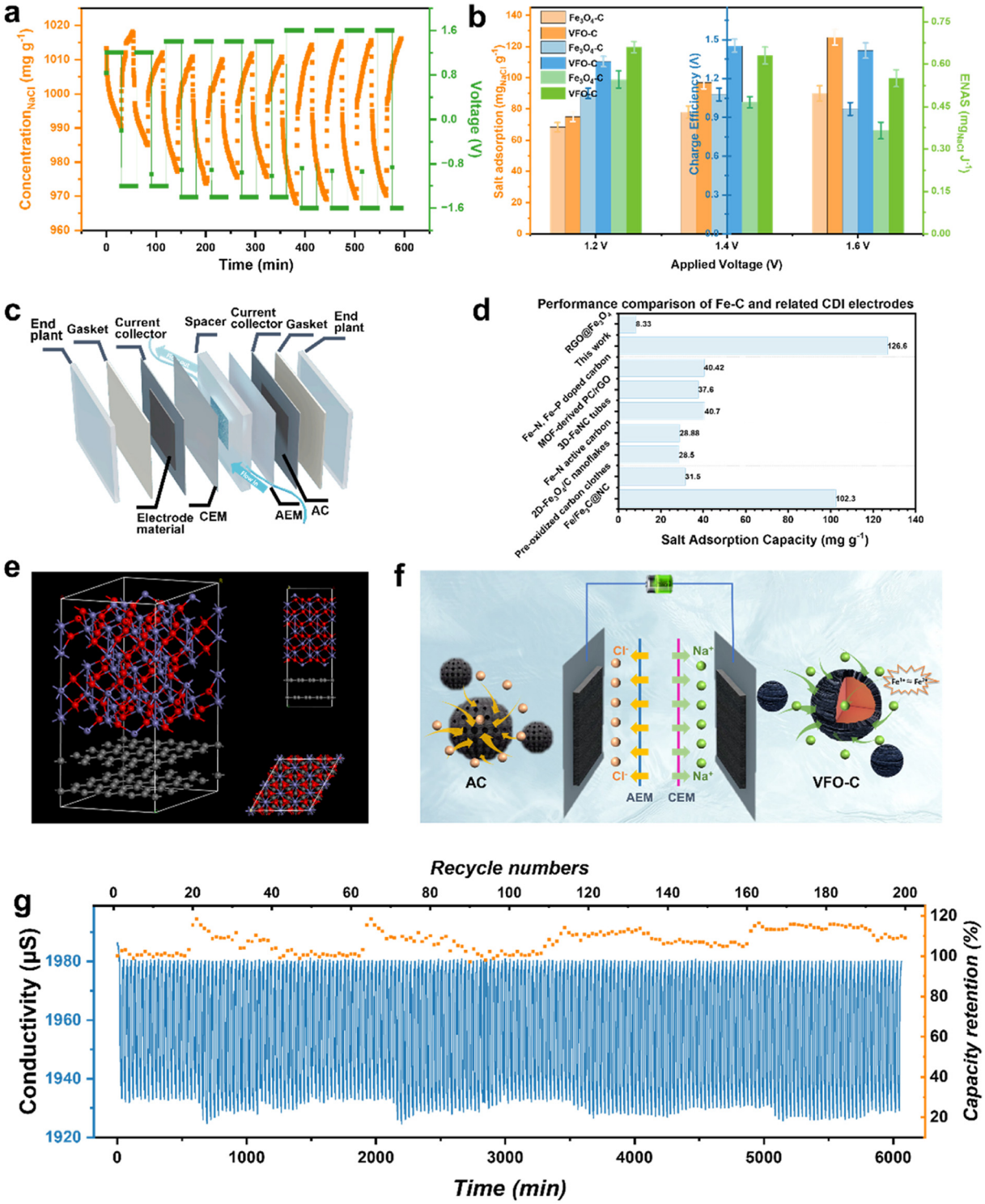

Fig. 4 (a) Concentrations responses of VFO-C electrode *versus* various cut-off voltage; (b) SACs, CEs and ENASs of VFO-C electrode and Fe_3O_4-C electrode at different cut-off voltages; (c) schematic illustrations of CDI devices; (d) performance comparison of VFO-C and related CDI electrodes;[50–57] (e) different perspectives on microstructure of VFO-C; (f) possible processes in both electrode materials during desalination; (g) the CDI cycling performances of VFO-C in 1000 mg L^{-1} NaCl at 1.4 V.

ion capture. In contrast, although higher voltages improve ion removal rates, they also exacerbate polarization effects and electrode kinetics, resulting in increased energy consumption.[58] The Ragone plot constructed based on these data (Fig. S5) illustrates the trade-off between energy density and power density.

A comparative summary of the desalination performance between VFO-C and Fe_3O_4-C was conducted based on key

metrics, including salt adsorption capacity (SAC), charge efficiency (Λ), and energy-normalized adsorption capacity (ENAS), as shown in Fig. 4b. Under identical voltage conditions, VFO-C consistently outperformed Fe_3O_4-C. Specifically, at 1.2, 1.4, and 1.6 V, the average SACs of VFO-C were approximately 75 ± 2, 97 ± 1, and 126.6 ± 2 mg g^{-1}, respectively, compared to 68 ± 2, 78 ± 2, and 90 ± 3 mg g^{-1} for Fe_3O_4-C. This enhanced performance is attributed to the presence of iron vacancy defects in VFO-C, which provide additional active sites, promote superior electrochemical reactivity, and enhance both the adsorption and desorption efficiency of Na^+ ions. Furthermore, the introduction of iron vacancies reduces the charge transfer resistance of Fe_3O_4, enabling faster reaction kinetics and a more rapid adsorption–desorption process. In terms of charge efficiency (Λ), the application of cation–anion exchange membranes effectively minimized the co-ion effect and mitigated electrode reversal issues, resulting in satisfactory and comparable charge efficiency values for both materials. As for ENAS, VFO-C demonstrated a pronounced advantage, with values of approximately 0.664 ± 0.002, 0.632 ± 0.002, and 0.552 ± 0.002 mg J^{-1} at 1.2, 1.4, and 1.6 V, respectively, in comparison to 0.546 ± 0.002, 0.465 ± 0.002, and 0.365 ± 0.002 mg J^{-1} for Fe_3O_4-C. These results suggest that although increasing voltage improves SAC, it also leads to higher energy consumption. Nonetheless, the superior energy efficiency of VFO-C across this voltage range highlights its distinct advantage in practical applications. The desalination unit incorporates a carefully designed internal structure to optimize electrode exposure and electrolyte transport as show in Fig. 4c. This design helps to achieve uniform current distribution and minimize electrode polarization, thereby improving desalination efficiency and cycling stability. To highlight the advantages of VFO-C, desalination performance with representative CDI electrodes reported have been compared in recent studies. For example, Fe/Fe_3C@NC delivered 102.3 mg g^{-1},[52] pre-oxidized carbon cloth 31.5 mg g^{-1},[51] and MOF-derived PC/rGO 37.6 mg g^{-1},[50] all significantly lower than the 126 mg g^{-1} achieved by VFO-C under similar conditions. These results clearly demonstrate the superiority of vacancy-engineered Fe_3O_4 integrated with biogas-slurry-derived carbon for high-efficiency CDI. The desalination mechanisms for this device also were explored during CDI process, AC located in the anode portion of the device, because of its high surface area and porous structure, helps to efficiently electrochemically adsorb ions from the electrolyte solution, which are removed by attracting the ions to pores and active sites during the dis/charging process. Unlike, the carbon layer located on the surface of VFO-C in the cathode portion of the device not only serves as a protection for Fe_3O_4 during dis/charging, but also the presence of iron vacancies facilitates the redox reactions between Fe^{3+} and Fe^{2+}, which contributes to its electrochemical activity in the CDI process and affects the electrochemical stability of the electrode, thus these contributes to its desalination performance. As shown in Fig. 4g, the electrode retained over 99% compared with initial desalination capacity after 200 consecutive cycles, exhibiting only a slight performance decay. This high retention clearly demonstrates the excellent regeneration ability and cycling stability of the composite. The remarkable stability can be attributed to the synergistic effects of iron-vacancy-enriched Fe_3O_4, which provides abundant intercalation-active sites with robust charge transfer capability, and the mesoporous carbon matrix derived from biogas slurry, which buffers the structural strain and enhances electronic conductivity.

2.4 Sodium removal mechanism analysis

To further elucidate the origin of VFO-C's enhanced Na^+ removal efficiency, DFT calculations were performed on both Fe_3O_4-C and VFO-C using the optimized theoretical model. Differential charge density maps were generated, where yellow regions indicate charge accumulation and green regions indicate charge depletion. As shown in Fig. 5d and e, the overall differential charge distributions for Na^+ adsorbed on Fe_3O_4-C and VFO-C are comparable, means that charge-transfer process exhibits a near balance in both the magnitude and direction of electron gain and loss. On the one hand, the increase in vacancies does not fundamentally change the reaction mechanism between Na^+ and the mesoporous carbon. However, the increased vacancy concentration modifies the Fe_3O_4–carbon interfacial interaction, which in turn changes the net charge transferred to the Na^+ ion.

The calculated adsorption energies (Fig. 5c) further support this conclusion: VFO-C exhibits an Na^+ adsorption energy of −0.53 eV, whereas Fe_3O_4-C binds Na^+ more strongly with an adsorption energy of −1.12 eV. Although the lower adsorption energy indicates weaker Na^+ binding, it simultaneously implies faster desorption kinetics and reduced energy barriers for ion release, which are critical for efficient electrosorption cycling. This interpretation is consistent with the migration energy barrier analysis (Fig. 5f), showing that VFO-C enables smoother Na^+ transport across the electrode–electrolyte interface. Such a balance between moderate adsorption strength and facile desorption is essential for achieving high desalination capacity while maintaining superior reversibility, long-term stability, and energy efficiency in CDI operation.

3 Economic benefit evaluation

Compared to direct land application and biological treatment, biogas-slurry nutrient recovery *via* CDI process was significant dominance in economic benefits and carbon reduction. The economic benefit was negative at $3.01 per m^3 and carbon emission was at 10.79 kg CO_2 m^{-3} based direct land application of biogass-slurry.[59] The economic benefit exhibited negatively at $7.68 per m^3 and carbon emission is achieved to 1.62 kg CO_2 m^{-3} based biological treatment, because the energy-intense nutrient removal also

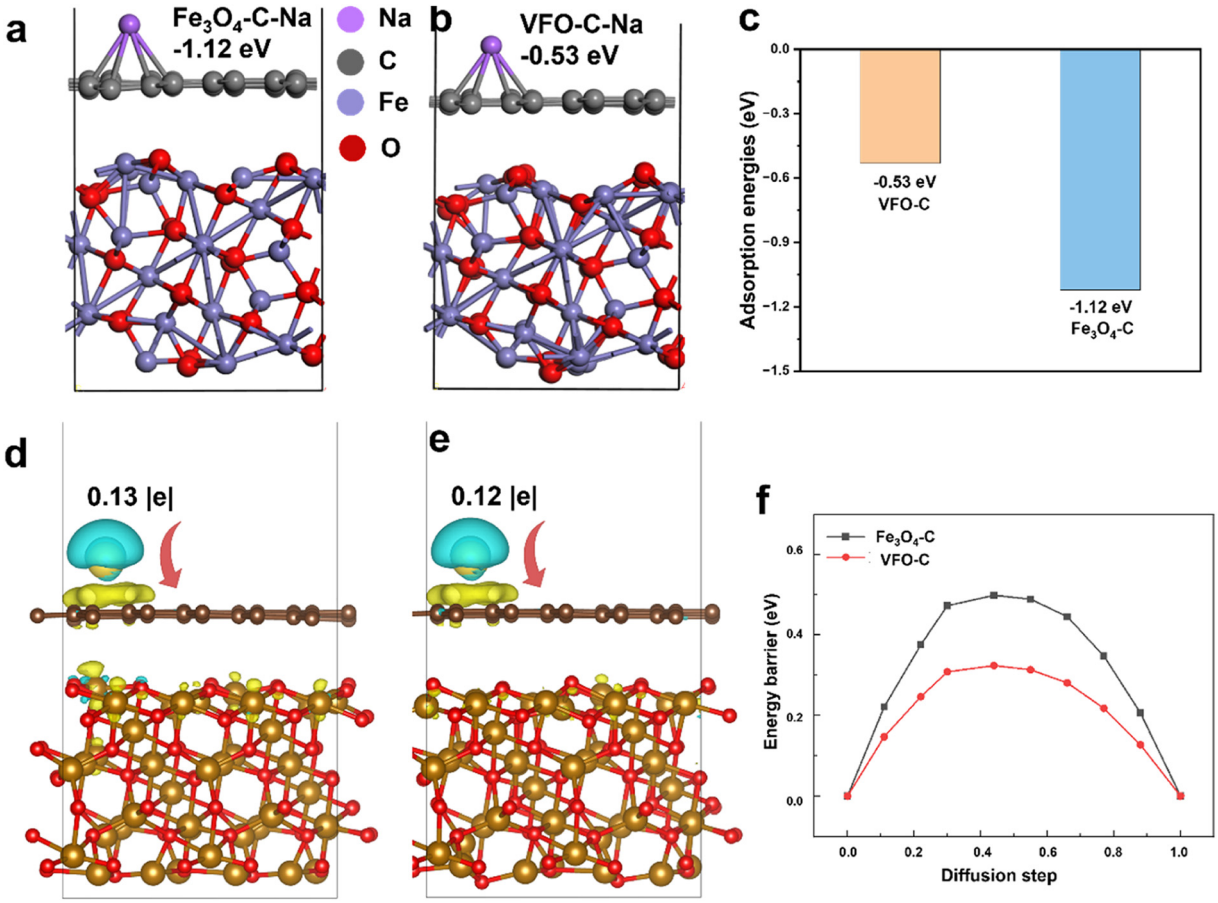

Fig. 5 (a) and (b) Adsorption model of Fe_3O_4-C and VFO-C surface adsorption of Na^+; (c) adsorption energy for different Na^+ adsorbed sites Fe_3O_4-C and VFO-C; (d) and (e) changes in electron density during the adsorption of Na^+ in Fe_3O_4-C and VFO-C are indicated by green and yellow colors, representing reductions and increases, respectively; (f) migration energy barriers of Na^+ in Fe_3O_4-C and VFO-C based on DFT calculations.

contributes to greenhouse gas emission of 0.9 kg CO_2 per kg N of treated wastewater based on biogas-slurry storage and farmland irrigation.[60]

For seawater desalination, costs depend on the technology employed, with reverse osmosis being one of the most commonly used methods. Recent estimates indicate that the operational cost of seawater reverse osmosis (SWRO) desalination ranges from \$0.50 to \$3.00 per m^3,[61] depending on the energy source and system efficiency. In high-salinity regions, such as the Arabian Gulf, the total dissolved solids (TDS) in the water are higher, leading to increased energy consumption and thus higher desalination costs. The combined use of biogas-slurry can effectively reduce operational costs, as it represents a reutilization of waste resources while simultaneously enhancing the environmental sustainability of processes such as seawater desalination or ion removal.

4 Conclusions

In this study, iron-vacancy Fe_3O_4 carbon composites were successfully prepared through an alkali etching and calcination process, exhibiting stable desalination properties. The strategy of introducing vacancies facilitated the rapid transfer of electrons and ions while increasing the exposure and utilization of more active sites. Furthermore, the incorporation of biogas slurry, an anaerobic fermentation byproduct, as the carbon source not only enhanced the electrochemical activity and environmental stability of the material during desalination tests, but also significantly reduced system costs by utilizing a "waste-to-waste" approach, wherein agricultural residual waste was employed for wastewater treatment. The results demonstrate that VFO-C exhibits excellent deionization performance, with an ion adsorption capacity of 126.6 mg g^{-1} at 1.6 V, and a capacity retention rate of over 99% after 200 cycles-outperforming previously reported CDI electrodes in both desalination capacity and cycle stability. In future work, this strategy could be leveraged as a selective pre-concentration step for subsequent valuable mineral extraction. This aligns perfectly with the emerging paradigm of transitioning desalination from a mere water purification process to a sustainable resource recovery platform.[62] This study provides a valuable reference for enhancing energy storage and environmental remediation technologies.

5 Experimental

5.1 Fabrication of the VFO-C electrode

A 3 : 1 molar mixture of $Fe(NO_3)_3{\cdot}5H_2O$ (1.51 g, 3 mmol) and $Al(NO_3)_3{\cdot}9H_2O$ (0.80 g, 3 mmol), along with urea (1.00 g, 16.7 mmol), was added dropwise to 100 ml biogas slurry over 10 min. During the addition and subsequent 12 h of stirring (25 °C, 300 rpm), biogas slurry was maintained to promote uniform adsorption of Fe^{3+}/Al^{3+}–urea complexes onto biomass particulates and facilitate *in situ* precipitation of metal hydroxides. It was transferred to the reaction kettle at hydrothermal 120 °C for 12 h. In the reaction, the decomposition of urea generates NH_3 and CO_2, NH_3 can form hydroxides with metal ions, and the organic components of biomass undergo a partial rearrangement, resulting in hydrothermal carbon, which is rich in metal hydroxides. The product was washed with deionized water and repeatedly centrifuged at 8000 rpm min^{-1} for 10 min until pH 7–8, and then dried in an oven at 60 °C.

For alkali activation, the dried precursor was mixed with NaOH under grinding and placed in an argon atmosphere tube furnace at 600 °C, 5 °C min^{-1} and annealed for 3 h. This process, on the one hand, carbonises the biomass into a carbonaceous skeleton, and on the other hand, NaOH etches the carbon framework and opens up a large number of mesopores at high temperatures. Residual inorganic species were removed by washing with 1 M HCl to neutral pH, the material was dried at 100 °C for 6 h, yielding the final mesoporous cation vacancies Fe_3O_4-decorated carbon composite (denoted VFO-C). A control sample (Fe_3O_4-C) was prepared using an identical procedure but omitting $Al(NO_3)_3{\cdot}9H_2O$ and the NaOH impregnation step.

5.2 Electrochemical performance evaluation and characterization

The electrochemical properties of VFO-C were evaluated using cyclic voltammetry (CV), galvanostatic charge–discharge (GCD), and electrochemical impedance spectroscopy (EIS) in a three-electrode cell configuration. EC-lab (biological SP-300) was used for all electrochemical measurements. CV scans were performed in a potential range of −0.6 V to 0.6 V *vs.* saturated calomel electrode (SCE) at a scan rate of 50 mV s^{-1}. GCD tests were conducted at a current density of 1 to 10 A g^{-1} over a potential window suitable for energy storage evaluation. EIS measurements were conducted over a frequency range of 0.01 Hz to 100 kHz with an AC voltage amplitude of 10 mV.

Surface elemental composition and oxidation states were analyzed on a Thermo Scientific ESCALAB 250Xi spectrometer using a monochromatic Al Kα X-ray source ($h\nu$ = 1486.6 eV) at 15 kV and 20 mA. Scanning Electron Microscopy (SEM) and SAED morphological analysis were performed on a JEOL JSM-IT500 SEM operated at 5–15 kV. Secondary-electron (SE) mode was used to capture surface topography, while back-scattered electron (BSE) mode provided compositional contrast. Transmission Electron Microscopy (TEM) and High-Resolution TEM (HRTEM). The instrument model used in this study was JEOL JEM-2100Plus from Japan, and Digital Micrograph (DM) software was used to analyze and process the TEM image test results.

5.3 Desalination performance testing

VFO-C and activated carbon were prepared by uniformly coating onto a graphite carbon paper (GCP) current collector. The desalination setup was a custom-built MCDI unit featuring a 4 cm × 4 cm cell, in which the cell compartments and electrodes were separated by cation- and anion-exchange membranes, respectively. VFO-C coated GCP as the cathode, activated carbon coated GCP as the anode (loaded with approximately 15–20 mg and had a thickness of 100 μm), respectively. NaCl solutions (1000 mg L^{-1}) were passed through the CDI cell at a flow rate of 15 mL min^{-1} using a peristaltic pump. The salt removal efficiency and capacitive behavior of the CDI cell were subjected to cycling charge–discharge operations at varying voltages offered by DC power supply, and data recorded by Mettler conductivity meter. Testing procedures and data processing for desalination performance are discussed in the section on SI.

5.4 Density functional theory calculations

the DFT as implemented in the Vienna *Ab initio* Simulation Package (VASP) in all calculations. The exchange–correlation potential is described by using the generalized gradient approximation of Perdew–Burke–Ernzerhof (GGA-PBE). The projector augmented-wave (PAW) method is employed to treat interactions between ion cores and valence electrons. The plane-wave cutoff energy was fixed to 400 eV. Given structural models were relaxed until the Hellmann–Feynman forces smaller than −0.02 eV $Å^{-1}$ and the change in energy smaller than 10^{-5} eV was attained. The vacuum thickness was set to be 25 Å to minimize interlayer interactions. During the relaxation, the Brillouin zone was represented by a Γ centered k-point grid of 1 × 1 × 1. Grimme's DFT-D3 methodology was used to describe the dispersion interactions among all the atoms in adsorption models.

Conflicts of interest

The authors declare no conflict of interest.

Data availability

The data that support the findings of this study are available from the corresponding author, [Professor Jie Ma, jma@tongji.edu.cn], upon reasonable request.

Supplementary information: the supplementary file contains [additional experimental data, methodological details, and supporting figures referenced in the main text.] See DOI: **https://doi.org/10.1039/d5im00117j**.

Acknowledgements

This research is supported by The National Natural Science Foundation of China (22276137, 52170087), and Innovation Research Team of Kashi University. We are also thankful to the anonymous reviewers for their valuable comments to improve this manuscript.

References

1 D. Su, H. Ahn and G. Wang, One-dimensional magnetite Fe_3O_4 nanowires as electrode material for Li-ion batteries with improved electrochemical performance, *J. Power Sources*, 2013, **244**, 742–746.
2 R. Yang, G. Zhou, C. Wang, Y. Liu, Y. Zhao, Y. Li, X. Fu, J. Chi, X. Chen and H. Fang, Insight into photo-fenton catalytic degradation of tetracycline by environmental friendly nanocomposite 1T-2H hybrid phases $MoS_2/Fe_3O_4/g\text{-}C_3N_4$, *J. Cleaner Prod.*, 2023, **383**, 135406.
3 Y. Xu, G. Wang, L. Zhu, W. Deng, C. Wang, T. Ren, B. Zhu and Z. Zeng, Desert beetle-like microstructures bridged by magnetic Fe_3O_4 grains for enhancing oil-in-water emulsion separation performance and solar-assisted recyclability of graphene oxide, *Chem. Eng. J.*, 2022, **427**, 130904.
4 H. Liu, S. Zhang, Y. Zhou, W. Yu, Y. Ma, S. Wang, Y. Chai and B. Dong, Dynamically stabilized electronic regulation and electrochemical reconstruction in Co and S atomic pair doped Fe_3O_4 for water oxidation, *Small*, 2023, **19**, 2301255.
5 X. Wang, X. Xing, H. Zhu, J. Li and T. Liu, State of the art and prospects of Fe_3O_4/carbon microwave absorbing composites from the dimension and structure perspective, *Adv. Colloid Interface Sci.*, 2023, **318**, 102960.
6 L. Li, G. Zhang, B. Wang and S. Yang, Constructing the Fe/Cr double (oxy)hydroxides on Fe_3O_4 for boosting the electrochemical oxygen evolution in alkaline seawater and domestic sewage, *Appl. Catal., B*, 2022, **302**, 120847.
7 L. Xu, S. Peng, L. Tang, Y. Zong, Y. Mao, M. Wu and D. Wu, Core–shell Fe_3O_4@C conductive additives for magnetic flow-electrode capacitive deionization: Reconstruction of charge percolation networks, *ACS ES&T Eng.*, 2023, **3**, 94–104.
8 L. Xu, L. Tang, S. Peng, Y. Mao and D. Wu, Magnetic array for efficient and stable Flow-electrode capacitive deionization, *Chem. Eng. J.*, 2022, **446**, 137415.
9 J. Rakhtshah, A comprehensive review on the synthesis, characterization, and catalytic application of transition-metal Schiff-base complexes immobilized on magnetic Fe_3O_4 nanoparticles, *Coord. Chem. Rev.*, 2022, **467**, 214614.
10 S. Xin, T. Liu, J. Li, H. Cui, Y. Liu, K. Liu, Y. Yang and M. Wang, Coupling of oxygen vacancies and heterostructure on Fe_3O_4 via an anion doping strategy to boost catalytic activity for lithium-sulfur batteries, *Small*, 2023, **19**, 2207924.
11 B. Bulut Kopuklu, A. Tasdemir, S. Alkan Gursel and A. Yurum, High stability graphene oxide aerogel supported ultrafine Fe_3O_4 particles with superior performance as a Li-ion battery anode, *Carbon*, 2021, **174**, 158–172.
12 Y. Li, B. Xue, S. Yang, Z. Cheng, L. Xie and Q. Zheng, Flexible multilayered films consisting of alternating nanofibrillated cellulose/Fe_3O_4 and carbon nanotube/polyethylene oxide layers for electromagnetic interference shielding, *Chem. Eng. J.*, 2021, **410**, 128356.
13 T. Vo, J. Gao and Y. Liu, Recent development and future frontiers of oxygen reduction reaction in neutral media and seawater, *Adv. Funct. Mater.*, 2024, **34**, 2314282.
14 D. Grumelli, T. Wiegmann, S. Barja, F. Reikowski, F. Maroun, P. Allongue, J. Balajka, G. Parkinson, C. Chen, Z. Wang, Y. Ikuhara, U. Diebold, K. Kern and J. Wintterlin, Electrochemical stability of the reconstructed Fe_3O_4 (001) surface, *Angew. Chem., Int. Ed.*, 2020, **59**, 21904–21908.
15 K. McKenna, F. Hofer, D. Gilks, V. Lazarov, C. Chen, Z. Wang and Y. Ikuhara, Atomic-scale structure and properties of highly stable antiphase boundary defects in Fe_3O_4, *Nat. Commun.*, 2014, **5**, 5740.
16 X. Liu, X. Yan, W. Liu, Q. Yan and M. Xing, Switching of radical and nonradical pathways through the surface defects of Fe_3O_4/MoO_xS_y in a Fenton-like reaction, *Sci. Bull.*, 2023, **68**, 603–612.
17 S. Guo, T. Koketsu, Z. Hu, J. Zhou, C. Kuo, H. Lin, C. Chen, P. Strasser, L. Sui, Y. Xie, M. Gu and J. Ma, Mo-incorporated magnetite Fe_3O_4 featuring cationic vacancies enabling fast lithium intercalation for batteries, *Small*, 2022, **18**, 2203835.
18 L. Peng, N. Yang, Y. Yang, Q. Wang, X. Xie, G. Sun Waterhouse, L. Shang, T. Zhang and G. Waterhouse, Atomic cation-vacancy engineering of NiFe-layered double hydroxides for improved activity and stability towards the oxygen evolution reaction, *Angew. Chem., Int. Ed.*, 2021, **60**, 24612–24619.
19 L. de Almeida, E. Oreste, J. Maciel, M. Heinemann and D. Dias, Electrochemical devices obtained from biochar: Advances in renewable and environmentally-friendly technologies applied to analytical chemistry, *Trends Environ. Anal. Chem.*, 2020, **26**, e00089.
20 P. Subbarao, T. da Silva, K. Adlak, S. Kumar, R. Chandra and V. Vijay, Anaerobic digestion as a sustainable technology for efficiently utilizing biomass in the context of carbon neutrality and circular economy, *Environ. Res.*, 2023, **234**, 116286.
21 J. Song, Y. Wang, S. Zhang, Y. Song, S. Xue, L. Liu, X. Lv, X. Wang and G. Yang, Coupling biochar with anaerobic digestion in a circular economy perspective: A promising way to promote sustainable energy, environment and agriculture development in China, *Renewable Sustainable Energy Rev.*, 2021, **144**, 110973.
22 L. Di, Q. Zhang, F. Wang, H. Wang, H. Liu, W. Yi, Z. Zhang and D. Zhang, Effect of nano- Fe_3O_4 biochar on anaerobic digestion of chicken manure under high ammonia nitrogen concentration, *J. Cleaner Prod.*, 2022, **375**, 134107.
23 L. Di, F. Wang, S. Li, H. Wang, D. Zhang, W. Yi and X. Shen, Influence of nano-Fe_3O_4 biochar on the methanation pathway during anaerobic digestion of chicken manure, *Bioresour. Technol.*, 2023, **377**, 128979.
24 Q. Ma, C. Zhong, J. Ma, C. Ye, Y. Zhao, Y. Liu, P. Zhang, T. Chen, C. Liu, B. Chu, W. Ma and H. He, Comprehensive study about the photolysis of nitrates on mineral oxides, *Environ. Sci. Technol.*, 2021, **55**, 8604–8612.

25 Z. Tong, X. Zhu, H. Xu, Z. Li, S. Li, F. Xi, T. Kang, W. Ma and C. Lee, Multivalent-ion electrochromic energy saving and storage devices, *Adv. Funct. Mater.*, 2024, **34**, 2308989.
26 F. Wu, S. Qiang, X. Zhu, W. Jiao, L. Liu, J. Yu, Y. Liu and B. Ding, Fibrous MXene aerogels with tunable pore structures for high-efficiency desalination of contaminated seawater, *Nano-Micro Lett.*, 2023, **15**, 71.
27 Y. Wang, T. Lian, N. Tarakina, J. Yuan and M. Antonietti, Lamellar carbon nitride membrane for enhanced ion sieving and water desalination, *Nat. Commun.*, 2022, **13**, 7339.
28 T. Gao, R. Zhao, Y. Li, Z. Zhu, C. Hu, L. Ji, J. Zhang and X. Zhang, Sub-nanometer Fe clusters confined in carbon nanocages for boosting dielectric polarization and broadband electromagnetic wave absorption, *Adv. Funct. Mater.*, 2022, **32**, 2204370.
29 Y. Liu, Z. Wu, M. Naschitzki, S. Gewinner, W. Schöllkopf, X. Li, J. Paier, J. Sauer, H. Kuhlenbeck and H. Freund, Elucidating surface structure with action spectroscopy, *J. Am. Chem. Soc.*, 2020, **142**, 2665–2671.
30 S. Kamari and A. Shahbazi, High-performance nanofiltration membrane blended by Fe_3O_4@SiO_2–CS bionanocomposite for efficient simultaneous rejection of salts/heavy metals ions/dyes with high permeability, retention increase and fouling decline, *Chem. Eng. J.*, 2021, **417**, 127930.
31 S. Naseem, C. Wu and K. Motora, Novel multifunctional Rb_xWO_3@Fe_3O_4 immobilized Janus membranes for desalination and synergic-photocatalytic water purification, *Desalination*, 2021, **517**, 115256.
32 B. Wang, K. Yang, B. Cai, J. Zhang, C. Wei and A. Zhou, A magnetic nanostructure PAC@Fe_3O_4 driven design toward Janus hydrogel achieves highly efficient solar water evaporation, *Chem. Eng. J.*, 2023, **465**, 142944.
33 H. Far, M. Hasanzadeh, M. Nashtaei, M. Rabbani, A. Haji and B. Hadavi Moghadam, PPI-dendrimer-functionalized magnetic metal–organic framework (Fe_3O_4@MOF@PPI) with high adsorption capacity for sustainable wastewater treatment, *ACS Appl. Mater. Interfaces*, 2020, **12**, 25294–25303.
34 Y. Mao, J. Liu, J. Sun, Y. Zhao, Y. An, L. Wu, H. Feng, B. Chen, R. Chen, K. Zhang, Y. Du and D. Yang, Elucidating the bioinspired synthesis process of magnetosomes-like Fe_3O_4 nanoparticles, *Small*, 2024, **20**, 2308247.
35 Y. Zhao, H. Zhang, X. Yang, H. Huang, G. Zhao, T. Cong, X. Zuo, Z. Fan, S. Yang and L. Pan, In situ construction of hierarchical core–shell Fe_3O_4@C nanoparticles–helical carbon nanocoil hybrid composites for highly efficient electromagnetic wave absorption, *Carbon*, 2021, **171**, 395–408.
36 Z. Li, H. Lin, S. Ding, H. Ling, T. Wang, Z. Miao, M. Zhang, A. Meng and Q. Li, Synthesis and enhanced electromagnetic wave absorption performances of Fe_3O_4@C decorated walnut shell-derived porous carbon, *Carbon*, 2020, **167**, 148–159.
37 C. Gao, Y. Su, X. Quan, V. Sharma, S. Chen, H. Yu, Y. Zhang and J. Niu, Electronic modulation of iron-bearing heterogeneous catalysts to accelerate Fe(III)/Fe(II) redox cycle for highly efficient Fenton-like catalysis, *Appl. Catal., B*, 2020, **276**, 119016.
38 S. Wang, P. Yang, X. Sun, H. Xing, J. Hu, P. Chen, Z. Cui, W. Zhu and Z. Ma, Synthesis of 3D heterostructure Co-doped Fe_2P electrocatalyst for overall seawater electrolysis, *Appl. Catal., B*, 2021, **297**, 120386.
39 Y. Fang, Y. Xue, L. Hui, H. Yu and Y. Li, Graphdiyne@Janus magnetite for photocatalytic nitrogen fixation, *Angew. Chem., Int. Ed.*, 2021, **60**, 3170–3174.
40 Y. Fang, Y. Xue, L. Hui, H. Yu, C. Zhang, B. Huang and Y. Li, Graphdiyne-induced iron vacancy for efficient nitrogen conversion, *Adv. Sci.*, 2022, **9**, 2102721.
41 C. Guo, X. Liu, L. Gao, X. Kuang, X. Ren, X. Ma, M. Zhao, H. Yang, X. Sun and Q. Wei, Fe-doped Ni_2P nanosheets with porous structure for electroreduction of nitrogen to ammonia under ambient conditions, *Appl. Catal., B*, 2020, **263**, 118296.
42 H. Cao, C. Liu, F. Cai, X. Qiao, A. Dichiara, C. Tian and J. Lü, In situ immobilization of ultra-fine Ag NPs onto magnetic Ag@RF@Fe_3O_4 core-satellite nanocomposites for the rapid catalytic reduction of nitrophenols, *Water Res.*, 2020, **179**, 115882.
43 L. Su, P. Wang, X. Ma, J. Wang and S. Zhan, Regulating local electron density of iron single sites by introducing nitrogen vacancies for efficient photo-Fenton process, *Angew. Chem., Int. Ed.*, 2021, **60**, 21261–21266.
44 N. Esfandiari, M. Kashefi, M. Mirjalili and S. Afsharnezhad, Role of silica mid-layer in thermal and chemical stability of hierarchical Fe_3O_4-SiO_2-TiO_2 nanoparticles for improvement of lead adsorption: Kinetics, thermodynamic and deep XPS investigation, *Mater. Sci. Eng., B*, 2020, **262**, 114690.
45 G. Divyapriya, I. Nambi and J. Senthilnathan, An innate quinone functionalized electrochemically exfoliated graphene/Fe_3O_4 composite electrode for the continuous generation of reactive oxygen species, *Chem. Eng. J.*, 2017, **316**, 964–977.
46 Y. Huang, Z. Xu, J. Mai, T. Lau, X. Lu, Y. Hsu, A. Chen, Y. Lee, Y. Hou and Y. Meng, Revisiting the origin of cycling enhanced capacity of Fe_3O_4 based nanostructured electrode for lithium ion batteries, *Nano Energy*, 2017, **41**, 426–433.
47 K. Wasiński, M. Walkowiak, P. Półrolniczak and G. Lota, Capacitance of Fe_3O_4/rGO nanocomposites in an aqueous hybrid electrochemical storage device, *J. Power Sources*, 2015, **293**, 42–50.
48 S. Pandey, S. Neupane, D. Gupta, R. Yadav and A. Yadav, Synthesis and application of Fe_3O_4 nanoparticles in electrochemical pseudocapacitor, *Emergent Mater.*, 2022, **5**, 1899–1906.
49 W. Xu, W. Zhong, C. Yang, R. Zhao, J. Wu, X. Li and N. Yang, Tailoring interfacial electron redistribution of Ni/Fe_3O_4 electrocatalysts for superior overall water splitting, *J. Energy Chem.*, 2022, **73**, 330–338.
50 W. Shi, C. Ye, X. Xu, X. Liu, M. Ding, W. Liu, X. Cao, J. Shen, H. Yang and C. Gao, High-performance membrane capacitive deionization based on metal–organic framework-

derived hierarchical carbon structures, *ACS Omega*, 2018, **3**, 8506–8513.

51 X. Zhao, Y. Zheng, Z. Zheng, Z. Guo, T. Sun, J. Qin, N. Qiu, Z. Zhang and W. Wen, Pre-oxidized ultramicroporous carbon cloth with ultrahigh volumetric capacity and ultralong lifespan for capacitive desalination, *npj Clean Water*, 2023, **6**, 71.

52 H. Gang, H. Deng, L. Yan, B. Wu, S. Alhassan, Y. Cao, D. Wei and H. Wang, Surface redox pseudocapacitance boosting Fe/Fe_3C nanoparticles-encapsulated N-doped graphene-like carbon for high-performance capacitive deionization, *J. Colloid Interface Sci.*, 2023, **638**, 252–262.

53 L. Chen, X. Xu, L. Wan, Y. Zhu, Y. Ling, R. Li, J. Duan and T. Zhai, Carbon-incorporated Fe_3O_4 nanoflakes: high-performance faradaic materials for hybrid capacitive deionization and supercapacitors, *Mater. Chem. Front.*, 2021, **5**, 3480–3488.

54 S. Liu, P. Zhang, Y. Wang, M. He, W. Zhang, Z. Xu and K. Li, Uniformly dispersed Fe–N active centers on hierarchical carbon electrode for high-performance capacitive deionization: Plentiful adsorption sites and conductive electron transfer, *ACS Sustainable Chem. Eng.*, 2023, **11**, 8847–8857.

55 X. Xu, J. Tang, Y. Kaneti, H. Tan, T. Chen, L. Pan, T. Yang, Y. Bando and Y. Yamauchi, Unprecedented capacitive deionization performance of interconnected iron–nitrogen-doped carbon tubes in oxygenated saline water, *Mater. Horiz.*, 2020, **7**, 1404–1412.

56 S. Liu, P. Zhang, J. Huang, C. Li, W. Zhang, Z. Xu, C. Lv and K. Li, Fe-N and Fe-P dual active centers in MOF-derived carbon electrode for efficient capacitive deionization: Abundant defects and superior electrochemical properties, *Sep. Purif. Technol.*, 2023, **326**, 124843.

57 H. Li, Z. Leong, W. Shi, J. Zhang, T. Chen and H. Yang, Hydrothermally synthesized graphene and Fe_3O_4 nanocomposites for high performance capacitive deionization, *RSC Adv.*, 2016, **6**, 11967–11972.

58 K. Zuo, K. Wang, A. Deshmukh, S. Jia, H. Guo, R. Xin, M. Elimelech, P. Ajayan, J. Lou and Q. Li, Multifunctional nanocoated membranes for high-rate electrothermal desalination of hypersaline waters, *Nat. Nanotechnol.*, 2020, **15**, 1025–1032.

59 T. Mdlambuzi, M. Tsubo and P. Muchaonyerwa, Short-term effects of selected organic fertilizer sources on carbon dioxide fluxes and soil quality, *J. Environ. Qual.*, 2021, **50**, 312–323.

60 S. Liu, T. Liu, S. Zheng, R. Wang and S. Sang, Evaluation of carbon dioxide geological sequestration potential in coal mining area, *Int. J. Greenhouse Gas Control*, 2023, **122**, 103814.

61 Y. Lim, K. Goh, M. Kurihara and R. Wang, Seawater desalination by reverse osmosis: Current development and future challenges in membrane fabrication – A review, *J. Membr. Sci.*, 2021, **629**, 119292.

62 T. Vo, Y. Ng, P. Thangasamy, R. Venkatramanan, W. Goh, J. Bu, J. Gao and Y. Liu, Sustainable carbon-negative mineral extraction from desalination brine, *Appl. Catal., B*, 2024, **357**, 124321.